university of groningen / faculty of science and engineering

Examining the effect of Bromide as an additive for Tin-Triiodide Perovskite Thin Films

Bachelor's Project Thesis

Niamh O'Shea Scanlan, S3336549, n.c.oshea.scanlan@student.rug.nl
Daily Supervisor: E.K. Tekeleburg
Examiners: M.A. Loi & L.J.A. Koster

Dedicated to David Scanlan, who never got to see this finished.

Abstract: Sn-perovskites are recently being considered as an alternative to toxic Pb-perovskites for use in solar cells but are failing to offer similarly high efficiencies. The use of additives can improve its performance, where SnF_2 is commonly used. However, SnF_2 can cause phase separation so this study examines the effects of adding various concentrations of the additive $SnBr_2$ to a tin-based perovskite formamidinium triiodide ($FASnI_3$) for use in hot carrier solar cells. $FASnI_3$ has shown to have long lived hot carrier light emission which contributes to higher solar cells efficiencies in an attempt to exceed the Shockley-Queisser limit. It was found that although hot-carrier emission was present in the samples with $SnBr_2$, the additive did not significantly improve performance and material quality of the perovskite. The photoluminescence, absorption spectra, scanning tunneling microscopy, and X-ray diffraction were examined to determine the material quality of each sample and it was found that the hot carrier lifetime was shortened by the additive both in the 3D and 2D/3D regimes.

Contents

1 Introduction

Solar cell research has been a large part of the green energy transition in an effort to reduce the negative environmental impacts of our energy usage. The material science behind solar cells is key in trying to improve their performance. Many materials comprise a solar cell photovoltaic (PV) but the fundamental materials of PVs are semiconductors. As seen in figure 1.1, GsAs and silicon have been the two highest preforming single junction PV devices over the past 50 years. Metal-halide perovskite solar cells (PSCs) are one branch of photovoltaics that are have recently shown promise compared to other PV devices. In the last decade, however, perovskites have reached as high as 25.7% for perovskite cells and 31.3% for perovskite/Si tandem cells [1][2]. This impressive fast growth could surpass silicon PVs and allow for perovskites to become the leading PV for solar cells in efficiency in the future. This trend is attributed to the fact that metal halide PVCs have the ability to harness the excess energy absorbed by the material to exceed the Shockley-Queisser limit by way of slowing the thermalization of highly excited carriers. This limit in single junction solar cells is around 33% [3].

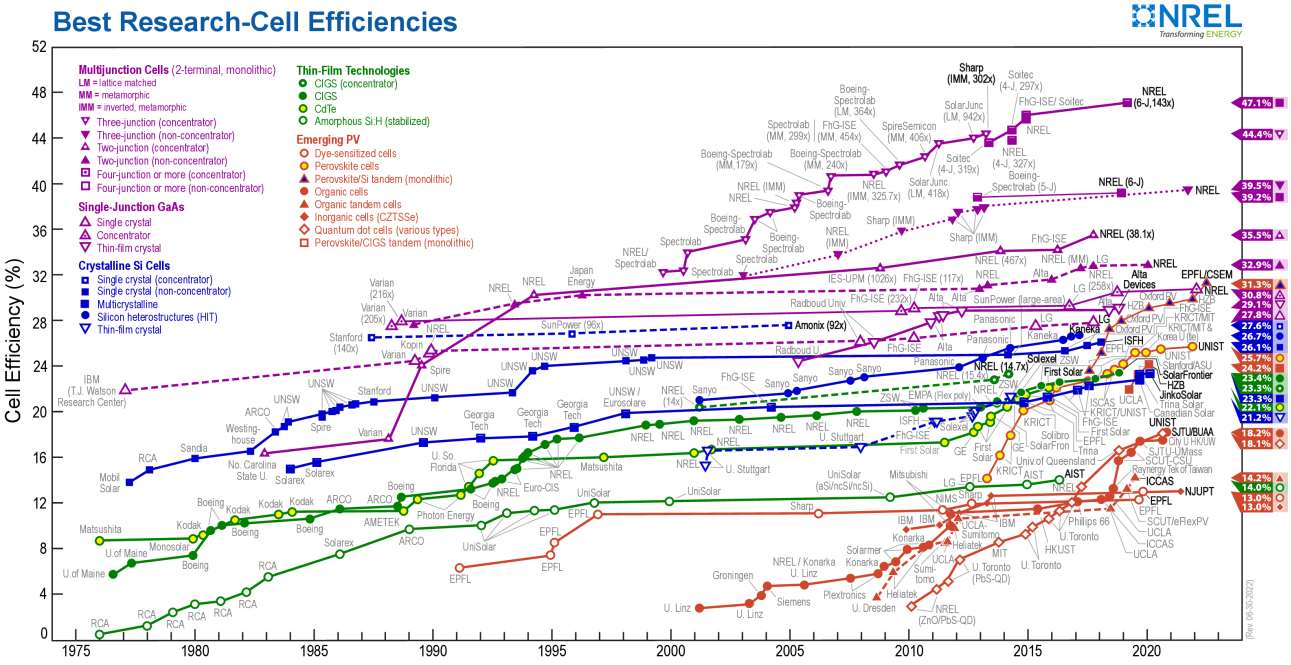

Figure 1.1: The trends of power conversion efficiencies of various types of solar cells. PSCs fall under the Emerging PV category and are denoted in red amongst other new PV cells. Taken from [2].

Metal-halide perovskites are defined by containing a metal like lead, caesium, or tin, as a cation and a halide as an anion with either an inorganic or organic cation in the chemical makeup, which forms a cubic structure at room temperature. Lead-based perovskites have shown the best power conversion efficiencies and have reached a record of 25.7% [2][4]. However, lead is toxic and is not a material that manufacturers are eager to work with due to the health risks and environmental concerns associated with lead. A less toxic alternative is tin but unfortunately, the highest recorded efficiency of tin based perovskites so far is 13.4% [5].

Although tin is widely considered less toxic than lead, the concerns about the toxicity of tin are still being investigated. Specifically the high absorption of the divalent form on tin, Sn^{+2}, contributes to toxicity by acidification which, as a result, causes gastric irritation in high doses [6][7]. However, these effects are nominal in smaller doses which makes it a safer alternative to lead which is comparatively toxic in small doses.

Sn-perovskites have some downsides that inhibit their material quality and, as a result, their power conversion efficiencies. Sn-perovskites are easily oxidised form $Sn^{2+} \longrightarrow Sn^{4+}$ and have a tendency to self-dope, making it an unstable material to work with and deteriorates rapidly when exposed to air. However, they still have potential, specifically due to their high absorption coefficient, excellent carrier diffusion length, and low defect density, all properties which contribute to higher power conversion efficiencies [8]. With more research and development to counteract the setbacks of these materials and enhance their potential, Sn-perovskites could reach efficiencies comparable to that of Pb-perovskites. High efficiency lead-free perovskites could lead the way for less toxic alternatives to PVCs.

The Sn-perovskite examined in this paper is formamidinium tin triiodide ($FASnI_3$), which is a 3D perovskite. Many methods to improve its performance have been previously studied. Some studies have added solvents such as liquid formic acid or pyrazine to the precursor solution during fabrication to improve crystalline growth and reproducibility [9][10]. Others have added small amounts 2D perovskite and SnF_2 to improve material quality and performance [11][12]. To further explore which additives can benefit $FASnI_3$ this study examines how $SnBr_2$ affects this perovskite since it has shown to improve power conversion efficiency at 4.3% compared to 3.4% for SnF_2 and 3.9% for $SnCl_2$ in the inorganic $CsSnI_3$ [13].

2 Theory

2.1 The Shockley-Queisser Limit & Hot Carriers

The key parameter of a PSC is its efficiency. The efficiencies of solar cells are limited by the Shockley-Queisser limit which puts the theoretical maximum efficiency of single junction solar cells at around 33% and is dependent on the band gap [3]. This limit is caused by energy loss from a number of different processes such as absorption losses due to photons with energy lower than the band gap and the fact that excess energy above the bandgap is lost. This loss of energy happens when the excited carriers relax to band edges and dissipate the potential energy to heat. One of the ways to overcome this limit is to extract carriers with an excess energy, so-called hot carriers, in the conduction band by slowing their thermalization.

These hot charged carriers which are generated when photons with energies higher than the band gap are absorbed [14]. The "hot" description comes from the fact that they exceed the mean thermal energy kT [15]. The relaxation (sometimes referred to as cooling) of the hot-carrier can happen through many different processes, which can happen simultaneously, and fall into two categories; radiative and non-radiative recombination. The former is characterized by the emission of a photon while the latter is most commonly characterized by the emission of a phonon (loss of thermal energy through lattice vibration). Radiative recombination processes, of relevance, can come in the form:

- (Free) exciton recombination (monomolecular);
- Band-to-band recombination (bimolecular).

The behaviour of these processes depends on the properties of the material, like the size and type of bandgap.

Some of the relevant non-radiative recombination processes come in the form:

- Multiphonon emission (Fig. 2.1(a)) (higher order recombination);
- Non-radiative auger recombination (Fig. 2.1(b)) (higher order recombination).

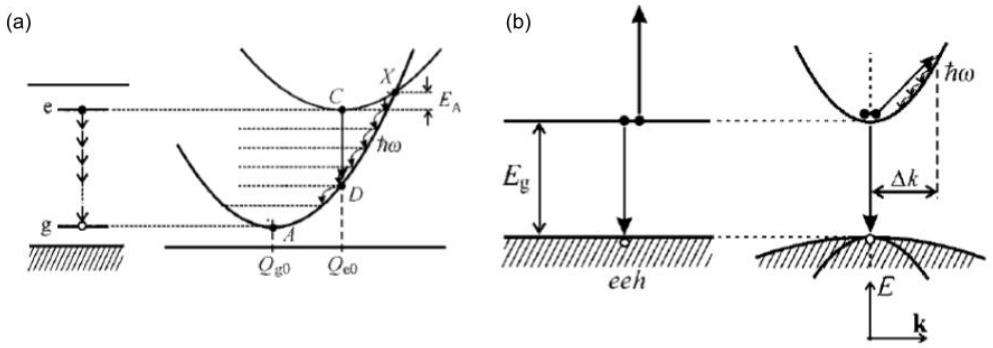

Figure 2.1: Some non-radiative decay processes; (a) multiphonon emission, (c) non-radiative auger recombination. The small arrows denote phonon decay while the longer arrows denote possible photon transitions. Taken from [16].

Whether the process is monomolecular (involving one carrier), bimolecular (two carriers), or of a higher order of recombination is relevant when it comes to excitation fluence. The excitation

fluence of a laser refers to the energy delivered per unit area and is directly related to the power of the laser. The fluence or power of the laser scales differently with the photoluminescence intensity depending on what type of recombination; linearly for monomolecular, quadratically for bimolecular, and so on.

Both the radiative decay time τ_R and non-radiative decay time τ_{NR} make up the total lifetime τ of the charged carrier which is determined by

$$\frac{1}{\tau} = \frac{1}{\tau_R} + \frac{1}{\tau_{NR}}. \tag{2.1}$$

These lifetimes are used to determine the luminescence quantum efficiency as

$$\eta = \frac{1/\tau_r}{1/\tau_r + 1/\tau_{nr}} \leqslant 1. \tag{2.2}$$

which is maximised at $\eta = 1$ for larger τ_{nr} non-radiative lifetimes.

Establishing a connection between the lifetime of the hot carriers and the luminescence quantum efficiency of the material gives insight into the material quality of the perovskite for use in solar cells. Luminescence measurements can be made with the perovskite layer alone without spending the time and resources to make a solar cell and measure its power conversion efficiency.

Non-radiative decay is considered to be a result of exciton-phonon coupling, an interaction between excitons and phonons that has an impact on the optical properties of a material. This interaction traps the exciton within the lattice causing a local polarization in the lattice. The resulting quasiparticle is referred to as a polaron. This polaron prevents the exciton and screens other excitons from cooling and recombining sometimes creating a phonon bottleneck (depicted in figure 2.2). As a result, the emission spectrum broadens. Studies on metal halide perovskites have actually suggested that exciton-phonon coupling enables the slow cooling behaviour of hot carriers because of the screening effect and the phonon bottleneck [17][18][19].

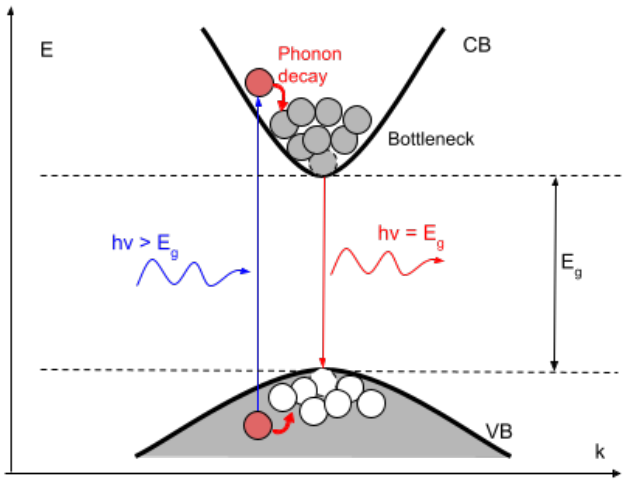

Figure 2.2: The formation of a so-called phonon bottleneck. Hot carriers must cool to the edge of the band before recombining and with other charged carriers in the way, the cooling is slowed down.

Another phenomenon that occurs in PVCs is band-edge filling where as carriers occupy the edges of the bands increasing the density of occupied states. The effect of this filling is the apparent optical bandgap is widened which causes a blue shift in absorption and emission spectra

know as the Burstein-Moss effect. This is an undesirable effect as it reduces the spectrum of light that a material can absorb which then, in turn, affects its performance in a solar cell.

Band-edge filling and phonon bottlenecks are both formations where particles accumulate at the edge of bands. The key difference between the phenomena is the difference in resulting effect; band-edge filling reduces absorption, a phonon bottleneck slows carrier cooling. The former is an undesirable and the latter, desirable, for use in solar cells.

2.2 Perovskite Crystal & Electronic Band Structure

Perovskites are materials with the structure ABX_3 where A and B are cations and X is an anion. Figure 2.3 shows the cubic lattice of a perovskite. This paper concentrates specifically on metal-halide-perovskites where A is a monovalent cation, B is a divalent metal and X is a halide. A can be organic like methylammonium or formamidinium, or an inorganic cation like ceasium. B is most often lead, tin or germanium and X is a halide like iodide, bromide or chloride. Perovskites are of interest to many because of their desirable bandgap, long hot-carrier lifetimes, and high absorption coefficient [20]. As a result of these characteristics, the efficiencies of devices with metal-halide-perovskites have jumped from 3.8% up to 25.5% in the last decade [1].

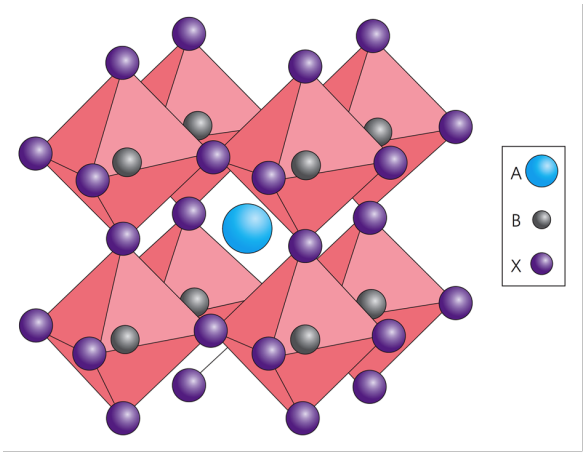

Figure 2.3: Crystal structure of perovskite. For metal-halide-perovskites A is a cation, B is a metal cation and X is a halide anion. Taken from [21].

Pb-based perovskites have taken the lead in terms of efficiencies of perovskite solar cells (25.5%) but the toxicity of lead makes in undesirable to work with due to health and environmental concerns. Sn-perovskites are a promising alternative to Pb since they have similar optical properties, high charge carrier mobilities and long hot carrier lifetimes and desirable bandgap (1.2-1.4 eV) [22]. One such Sn-perovskite is $FaSnI_3$ which has shown significantly long hot-carrier lifetimes, making it a promising candidate for hot carrier solar cells [12]. Figure 2.4 shows both a closer look at the crystal structure and the band structure of $FaSnI_3$.

The bond angles of $FASnI_3$ depend heavily on temperature which in turn affects the bandgap. At room temperature, $FASnI_3$ has cubic crystal structure but at lower temperatures can also have tetragonal or orthorhombic structure [24][25]. Despite the dependency on temperature, the bandgap, in any crystal configuration, is a direct bandgap. A direct bandgap is more desirable for use in solar cells because it more readily absorbs photons compared to indirect bandgaps, which require the absorption or emission of a phonon to absorb photons.

Perovskites can be formed in multiple dimensions. The repeating structure found in figure 2.4 forms a 3D perovskite. Thin layers of this structure with cation spacers between each layer

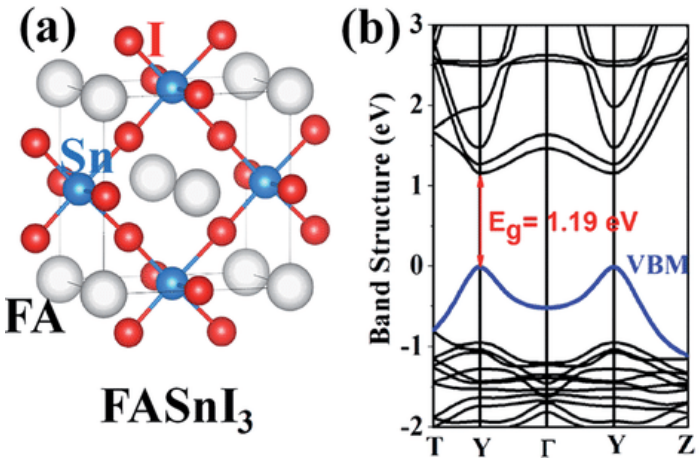

Figure 2.4: The (a) crystal structure and (b) band structure of $FASnI_3$. Taken from [23].

form a 2D perovskite. The spacer is formed when A is a large cation, so by adding a small about of a large cation to the main perovskite, a 2D/3D perovskite can be made. In this case, phenethylammonium (PEA), which is significantly larger than formamidinium (FA) is added to the perovskite. 2D and 2D/3D peroskites have found to be more stable long-term and have higher power conversion rates compared to 3D perovskites [26].

Since Sn-based perovskites have a tendency to self p-dope, the Burstein-Moss effect often shows up in it's absorption profile [12]. Doping can cause this excess concentration of one type of charged carrier. This effect can have adverse effects on the material quality and it inhibits absorption since only photons with more energy than this apparent bandgap can be absorbed. Additives like SnF_2 have shown to reduce this effect by mitigating the formation of tin vacancies which reduces the hole density caused by doping [27].

2.3 Strategies to Improve Performance

Sn-based perovskites have some characteristics which negatively affect their function in solar cells; instability due to oxidation, poor crystalline quality, low solar cell efficiency etc [22]. Researchers try to achieve an ideal state of the material through a number of adjustments; from adjusting the solvent composition [10] to changing the crystal dimension by adjusting the chemical composition [12].

As Sn^{2+} has the tendency to oxidise to Sn^{4+}, SnF_2 is often used as an additive to combat these problems, however, it can induce a phase separation on the surface of the perovskite if there is an excess [10][28]. Due to the issue of phase separation, different and better additives are needed. As previously mentioned, Heo *et al* found that SnF_2 similarly improves the material quality of $CsSnI_3$. In fact, the study found that $SnBr_2$ is even more effective in regards to stability over time and high solar cell efficiency [13]. So this study makes an effort to find whether $SnBr_2$ can similarly benefit $FASnI_3$ as an additive.

3 Experimental Methods

To examine the effect of $SnBr_2$ on formamidinium tin-triiodide, two types of the perovskite were made, a 3D and 2D/3D structure perovskite, each with different concentrations of $SnBr_2$; 5%, 7%, 10%, 15%, and 20%. Due to the nature of the lengthy fabrication process, these samples were made in two batches, one with 5%, 7%, and 10% of $SnBr_2$ and a second with the pristine 3D perovskite and 15% and 20% of $SnBr_2$. For comparison, each batch was made with a pristine sample of a composition that is well studied, both as a fully 3D perovskite and a 2D/3D perovskite: $FASnI_3$ with 10% SnF_2 [12]. The whole fabrication process was done in a N_2 filled glovebox and the samples were stored under N_2 atmosphere.

3.1 Fabrication: Solution

Formamidinium iodide (Sigma Aldrich, anhydrous, $\leq 99\%$), phenethylammonium iodide (Sigma Aldrich, 98%), tin (II) iodide (Alfa Aeser, ultra dry, 99.999%), tin (II) fluoride (Sigma Aldrich, 99%), and tin (II) bromide (Sigma Aldrich, $55.4 - 59.4\%$ Br basis) were the starting precursors used, which were either in (crystalline) powder or bead form. They were measured out using an electric balance and dissolved in a 300 µL solution of dimethylformamide (DMF) and dimethyl sulfoxide (DMSO) in a ration of 4:1, DMF:DMSO. The solutions were stirred overnight and spincoated the next day. Table 3.1 shows the molarity of each substance within each sample of 3D perovskite and the nicknames for each sample. SnF refers to the pristine sample.

Name	SnF	SnBr 5%	SnBr 7%	SnBr 10%	SnBr 15%	SnBr 20%
FAI	1 M	1 M	1 M	1 M	1 M	1 M
SnI_2	1 M	1 M	1 M	1 M	1 M	1 M
SnF_2	0.1 M	-	-	-	-	-
$SnBr_2$	-	0.05 M	0.07 M	0.1 M	0.15 M	0.2 M

Table 3.1: Molarity of each 3D perovskite.

To create a 2D/3D structure, a small amount phenethylammonium iodide (PEAI) was added to the solutions which otherwise went through an identical fabrication process as the 3D perovskites. Table 3.2 shows the specific molarities of each material for each solution.

Name	SnF	SnBr 5%	SnBr 7%	SnBr 10%
PEAI	0.08 M	0.08 M	0.08 M	0.08 M
FAI	0.92 M	0.92 M	0.92 M	0.92 M
SnI_2	1 M	1 M	1 M	1 M
SnF_2	0.1 M	-	-	-
$SnBr_2$	-	0.05 M	0.07 M	0.1 M

Table 3.2: Molarity of each 2D/3D perovskite.

3.2 Fabrication: Substrate cleaning procedure

Glass substrates (3x3cm) were first manually cleaned with warm soapy water for 30 seconds, 3 times. Then the substrates were sonicated for 10 minutes, twice, in deionised water, acetone, and isopropyl alcohol, respectively, refreshing the solvent each time. After this process, the substrates were dried in an oven at 140 °C for 10 minutes.

3.3 Fabrication: Spin-coating

Before spincoating the substrates were treated in a UV-ozone oven for 20 minutes. This treatment only stays in effect for 15 minutes so special attention was paid to make sure the samples were spincoated within 15 minutes of the treatment. 100 µL of perovskite solution was placed on the substrate and was spun for 60s at 4000 rpm with a 2000 rpm ramp up. After 15s of the 60s, 500 µL of antisolvent (diethyl ether) was dropped onto the sample without stopping the spincoater. The samples were then annealed on at hotplate of 70 °C for 20 min. Figure 3.1 demonstrates this procedure.

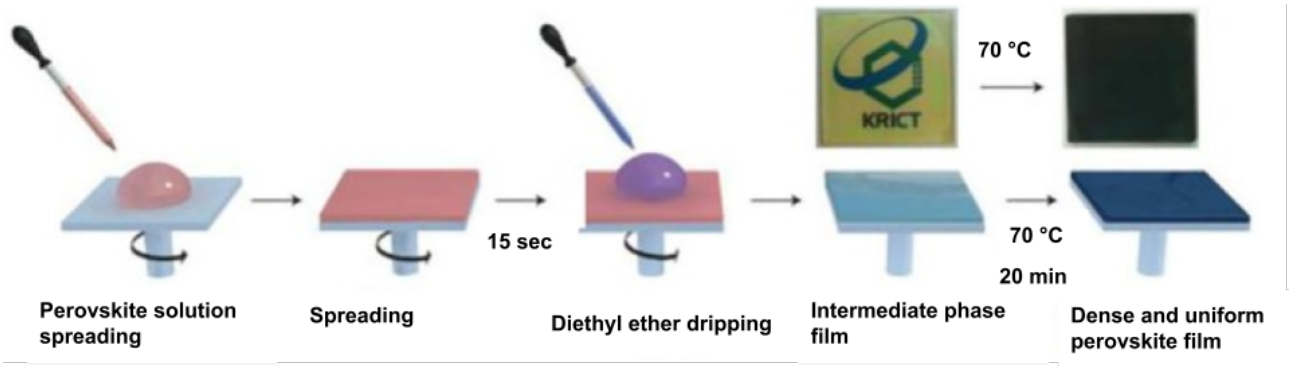

Figure 3.1: The various steps involved in the spincoating precedure. Figure adapted from [29].

3.4 Absorbance Spectroscopy

Ultraviolet-visible (UV-vis) absorption spectroscopy was used to obtain the absorption spectra of the various samples fabricated. A UV-vis absorption spectrometer compares the absoprtion of a sample with that of a reference (in this case a glass slide) to find the absorption spectrum of the sample alone. A Shimadzu 3600 UV-vis NIR spectrometer was used to record the absorption spectra between 400 nm and 1200 nm. Samples were held in a nitrogen filled sample holder during the measurement. Table 3.3 shows the settings for each measurement.

Scan speed	Medium	Detector Unit	Direct
Sampling interval	1.0 s	Source Lamp	WI
Measuring mode	Absorbance	Time constant	0.1 s
Slit width	8.0 nm		

Table 3.3: Settings used in the Shimadzu 3600 UV-vis NIR spectrometer.

3.5 Photoluminescence Spectroscopy

The samples were excited at 3.1 eV (400 nm) using the second harmonic of a mode-locked Ti:sapphire laser, specifically a Mira 900 series laser by Coherent. The spread of the excitation beam was reduced by an iris and focused with a 150 mm focal length lenses. The intensity of the laser was adjusted using a variable neutral density filter. Achromatic doublets, 425 nm and 435 nm longpass filters were placed in the collection beam path to collect the photoluminescence. Again a nitrogen filled sample holder was used to prevent exposure to oxygen during the measurements. Figure 3.2 shows the setup of the experiment. For high power laser measurements neutral density filters were placed between the sample and the collimating lenses to protect the camera.

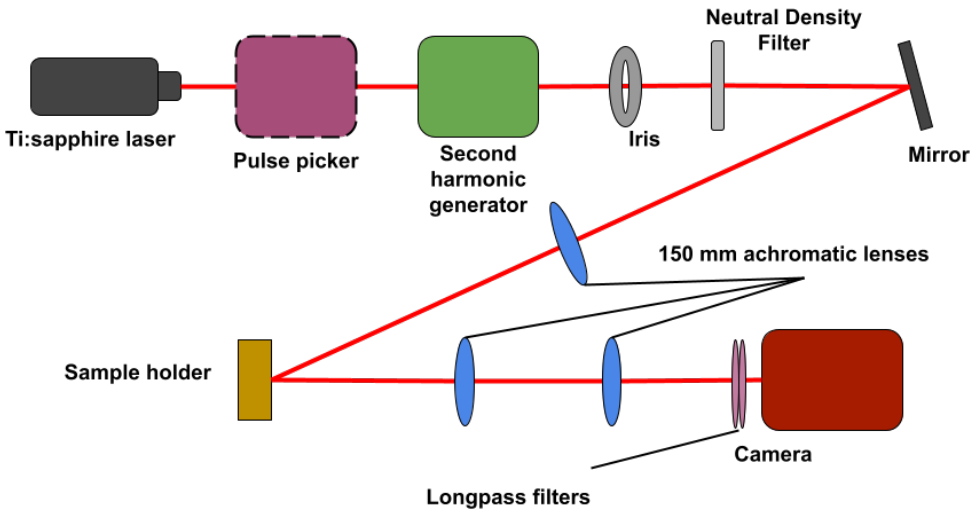

Figure 3.2: A schematic of the optical setup for the PL measurements.

Two aspects of photoluminescence excitation were measured/determined: the Steady State and the Time Resolved. Steady-state spectra were recorded with a Hamamatsu EM-CCD camera (in the range of visible light) and are a measurement of the time-integrated intensity of the fluorescence under constant excitation. The Time-Resolved spectra measure the time-dependent intensity of the of the fluorescence immediately after excitation to determine the lifetime of excited particles. Time-resolved spectra were taken with a set of Hamamatsu streak cameras working in the visible range which has two modes: synchroscan (up to 2000 ps) and single sweep (up to 1 ms), depending on the required time resolution. Since the single sweep has wider time ranges, the time between each pulse needs to be wider. An optical pulse picker (represented in Figure 3.2 by a pink box with a dashed outline) was used to adjust the repetition rate of the exciting pulses in order to measure using the single sweep mode.

3.6 X-Ray Diffraction

X-Ray Diffraction (XRD) is used to obtain information about the crystal structure of materials such as the lattice parameters and crystallographic planes. The sample is exposed to X-rays which interact with the atoms within the structure of the sample and the resulting diffraction subsequently produces a characteristic X-ray spectrum. The setup in figure 3.3 shows the orientation used in this experiment which is referred to as a Bragg-Brentano geometry. The measurement taken is referred to as a $2\theta - \theta$ scan. In this setup, the X-ray spectra are measured as a function of the angle at which the detector is, 2θ. The relationship between the order of diffraction n, wavelength λ, the lattice spacing d, and the angle of incidence θ is described by Bragg's Law:

$$n\lambda = 2dsin(\theta) \tag{3.1}$$

$2\theta - \theta$ scans allow us to identify the phases that are present in the material and determine the out-of-plane lattice parameter. The diffractometer finds high intensity peaks at various angles which denotes the presence of a crystal plane. Using Bragg's Law, the lattice spacing d can be determined from the angle at these peaks. More information on the crystallographic phases of the material can be found by comparing d with the lattice constants of the structure.

Spectra were measured on a Bruker D8 Advance X-ray diffractometer with a Cu K_α source ($\lambda = 1.54$ Å) and a Lynxeye detector.

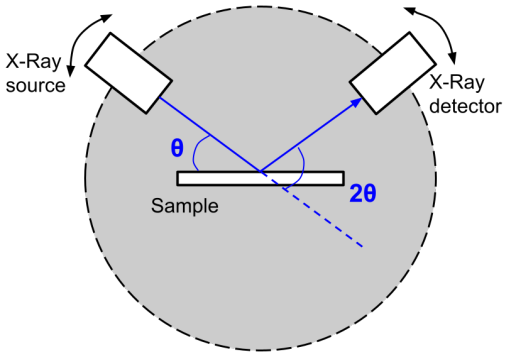

Figure 3.3: An XRD setup depicting the angle 2θ that is recorded.

3.7 Scanning Electron Microscope

A Scanning Electron Microscope (SEM) is a microscope that uses a beam of electrons to probe the surface of a sample to obtain an image of the surface of the sample. Using electromagnetic lenses, a beam of electrons is focused onto the sample. High-energy backscattered electrons and low-energy secondary electrons are then emitted from the sample. Depending on the setup, there is either a backscattered electron detector and a secondary electron detector or both. The detectors create an image of the topography from the intensity and position of the scattered electrons. Samples must be conductive so silver paste was applied to the samples in preparation for SEM measurements. The images were taken in air on a Nova NanoSEM 650 at an accelerating voltage of 15 kV.

4 Results & Discussion

4.1 SEM

Figure 4.1 shows SEM images of two batches, one that was exposed to air and one that was not. While the batches had different concentrations of $SnBr_2$, examining them side by side can present some interesting details on how the morphology of this perovskite is affected by exposure to air. The dark spots with outlines in white are pinholes while the grey shapes are the crystallites. The bright white structures, apparent in SnBr 5%, SnF 10% (d), SnBr 15%, and SnBr 20%, are precipitates that could possibly be due to phase separation from excess additive since this is also an issue with high concentration SnF_2 in $FASnI_3$. However, these precipitates could also be fully bromide perovskite. Evidence for this is found in the SnBr 20% sample (figure 4.1(f)) where there is a presence of lighter-coloured crystal formations surrounding the precipitates. These lighter-coloured crystals could be a bromide perovskite.

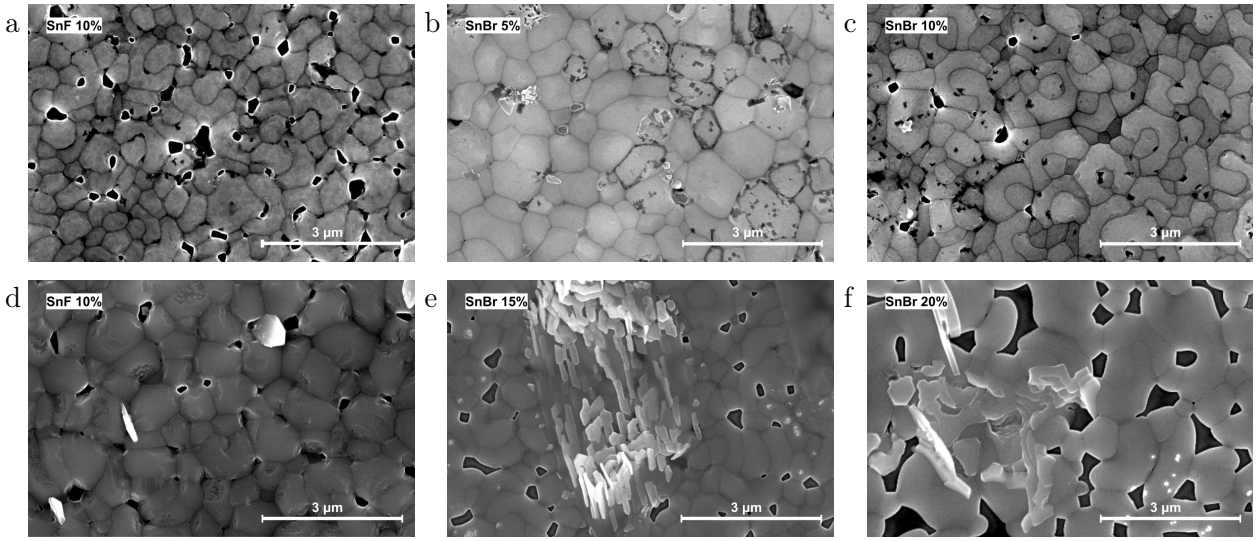

Figure 4.1: SEM images for both batches; a-c was one batch accidentally exposed to air, d-f was a second batch not exposed to air. Both batches include a pristine SnF 10% sample for batch-to-batch comparison. Courtesy of Matteo Pitaro.

Pinholes are abundant in the SnF 10% air-exposed sample and are least numerous in the SnBr 5%, despite the sample also being exposed to air. In fact, the SnBr 5% sample has the optimum morphology, with the least number of pinholes, large grain size, and fewer precipitates, all properties that improve electron and hole transport. These promising findings could indicate that $SnBr_2$ is a more beneficial additive to better resistance to ambient atmosphere compared to SnF_2. Pinholes and precipitates are undesirable features to have in a solar cell material as they inhibit charge transport and could decrease the efficiency of the device. Larger grain size, however, is indicative of the opposite; improved efficiency [30].

4.2 Photoluminescence Spectra

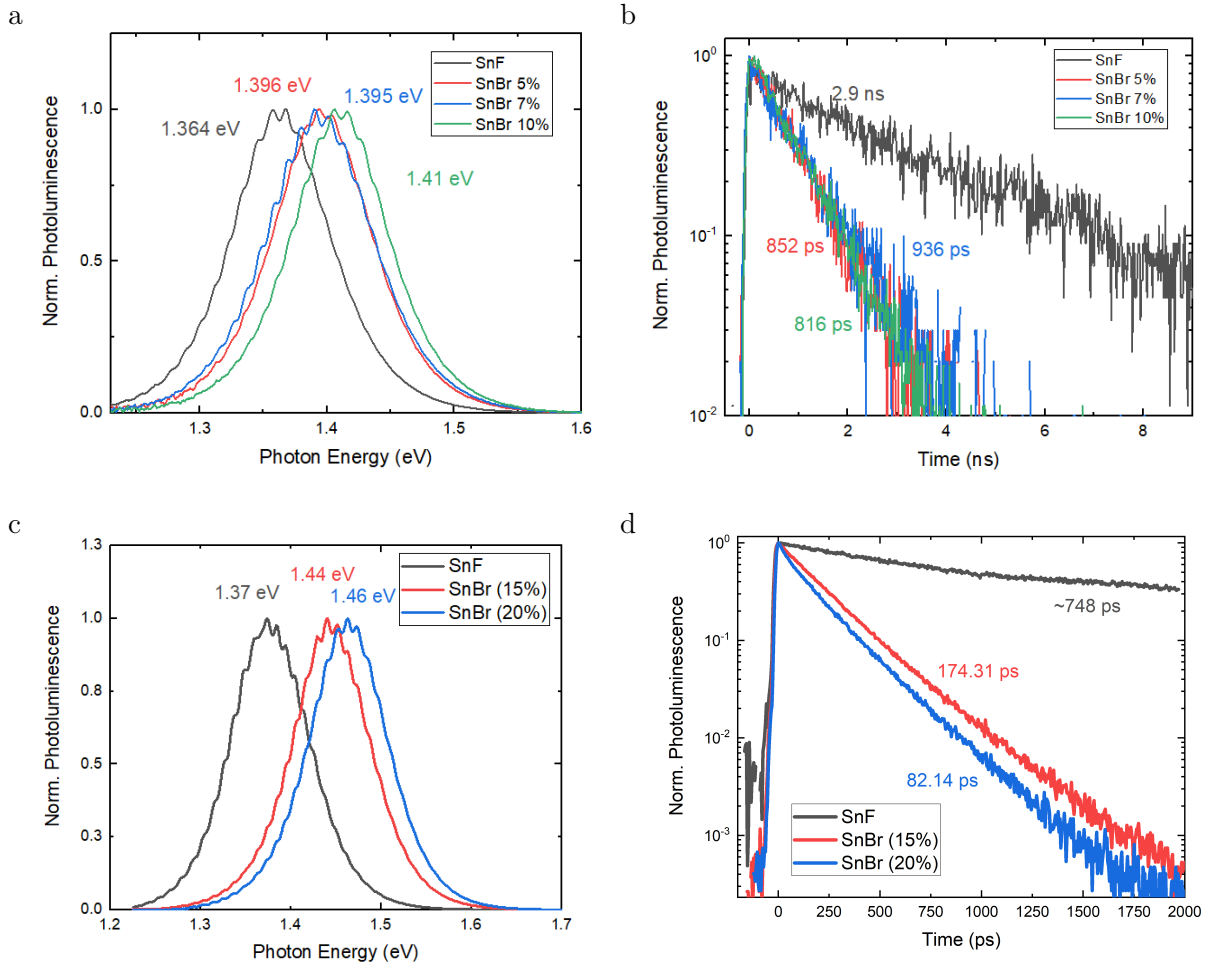

Figure 4.2: Steady state (a,c) and time-resolved (b,d) for two batches of 3D perovskite. Single sweep mode was used for b as Synchroscan was used for d, hence the different time scales.

Figure 4.2(a) shows the steady state photoluminescence of the batch with SnBr 5%, 7%, 10% with band gaps 1.364, 1.396, 1.395, and 1.41 eV respectively. There is an apparent blue shift in the SnBr samples compared to the SnF control. In fact, the SnBr 10% has a band gap of 1.41 eV, which reaches the limit of what is consider an ideal band gap for Sn-I-based perovskites (1.2-1.4 eV) [22]. This blue shift could be as a result of the Burstein-Moss effect (which is inhibited by SnF_2) or by contribution of the $SnBr_2$. The bromide perovskite $FASnBr_3$ has a bandgap of 2.4 eV, a much wider bandgap, so bromide could be widening the bandgap of $FASnI_3$ [31].

Figure 4.2(b) shows the time-resolved photoluminescence of the first batch of samples; 2.9 ns for SnF, 852 ps, 936 ps, and 816 ps for SnBr 5%, 7% and 10% repectively. As is visible from the graph, the lifetimes of the samples with $SnBr_2$ added are significantly shorter than the lifetime of just the SnF sample. A shorter lifetime indicates that the excited carriers lose the carrier population very quickly and thus with a shorter lifetime the SnBr samples do not have as high a quality as the SnF_2, as previously outlined in section 2.1.

In figure 4.2(c,d) similar results are shown for a second batch of samples with higher concentrations of SnBr, where there appears to be a trend of the material quality worsening as concentration increases. In Figure 4.2(d) the carrier lifetimes of the high concentration SnBr

samples are so short that the measurement had to be taken in a smaller time frame, which affected the ability to accurately determine the carrier lifetime of the control SnF sample.

From these results it can be assumed that SnBr is not a better alternative to SnF but that the optimal concentration of $SnBr_2$ appears to be 7% as it has the longest lifetime of 936 ps.

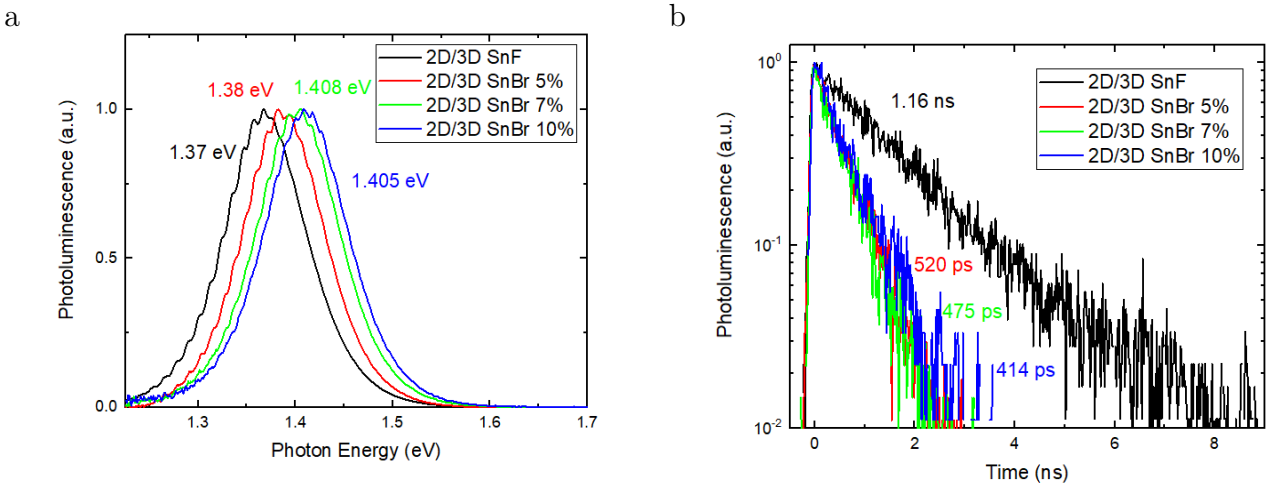

Figure 4.3: Steady state (a) and time-resolved (b) spectra for 2D/3D perovskites.

A similar result is found for the 2D/3D perovskites. Figure 4.3 shows that the samples with SnBr have a blue shifted band gap and shorter carrier lifetimes. The steady state for the 2D/3D perovskites spectra show a similar trend of the band gap reaching 1.4 eV with higher concentrations of $SnBr_2$. The time-resolved spectra again show shorter lifetimes for samples with $SnBr_2$ but it also shows a shorter lifetime for the pristine sample with SnF_2 compared to the pristine sample of the 3D perovskite. Previous studies have shown that this 2D/3D structure perovskite offers longer excited carrier lifetimes [12]. This may be an indication that this specific batch of 2D/3D perovskites may have an lower material quality than is expected or possible, however, it confirms that $SnBr_2$ performs worse than SnF_2 as an additive to improve carrier lifetimes in $FASnI_3$.

4.2.1 Hot-Carriers

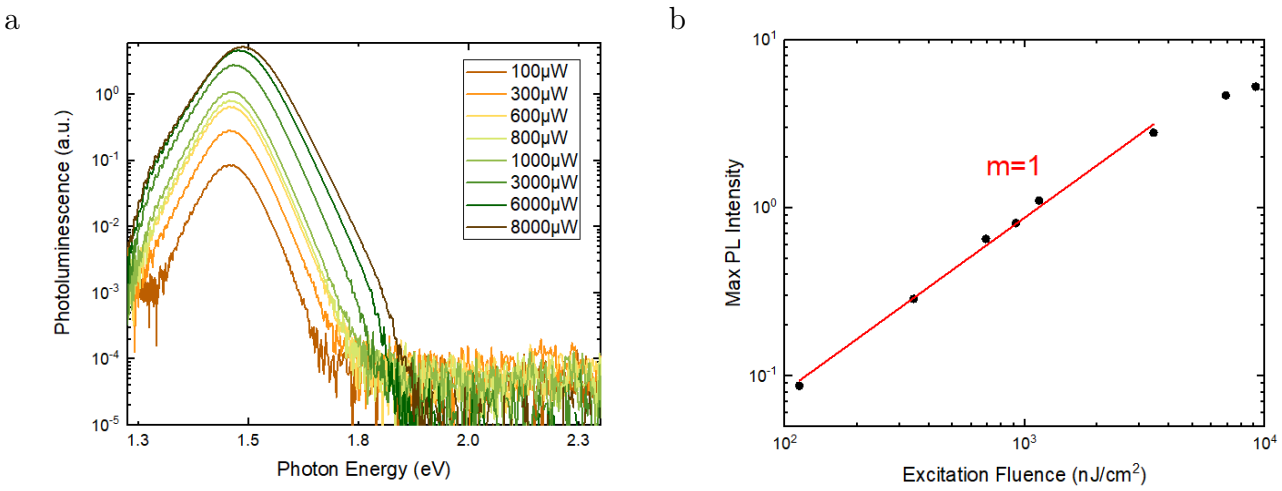

Figure 4.4: The (a) steady state spectra at a range of powers and (b) the max height at each excitation fluence (energy delivered per unit area) for the 3D SnBr 20% perovskite.

The time-resolved spectra measures the radiative lifetime of the excited carriers within the material. However, it does not give direct information on the kind of carriers present and the processes they go through. Examining the material response to a high power of the laser can provide more information. Figure 4.4(a) shows that as power is increased the peak slightly shifts to a higher energy.

Fang *et al* has shown this to be an indicator for the presence of slow hot carriers relaxation [32]. This study has also shown that a linear relation of the power dependence is attributed to recombination of excited electrons with the holes present due to the self-doping nature of the $FASnI_3$. The slope of this linear relation is 1 suggesting that monomelecular processes dominate the relaxation within the material. Fang *et al* also found that this slope doesn't extend to the higher powers which was attributed to the presence of Auger processes which are higher order processes. This change of slope is present in figure 4.4 suggesting that these higher order process are present in samples with $SnBr_2$ at high powers.

The SnBr 20% sample shows presence of hot carriers and the expected recombination processes for $FASnI_3$. The presence of hot carriers, however, are only seen at high powers which is not ideal for use in PSCs.

4.3 Absorbance Spectra

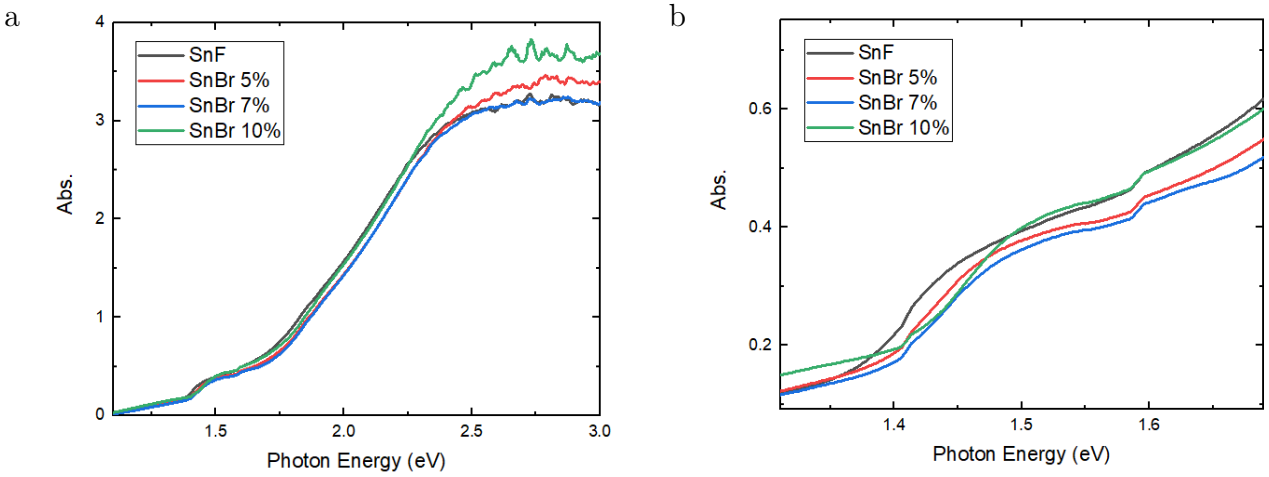

Figure 4.5: Absorbance spectra for the first batch of 3D perovskites.

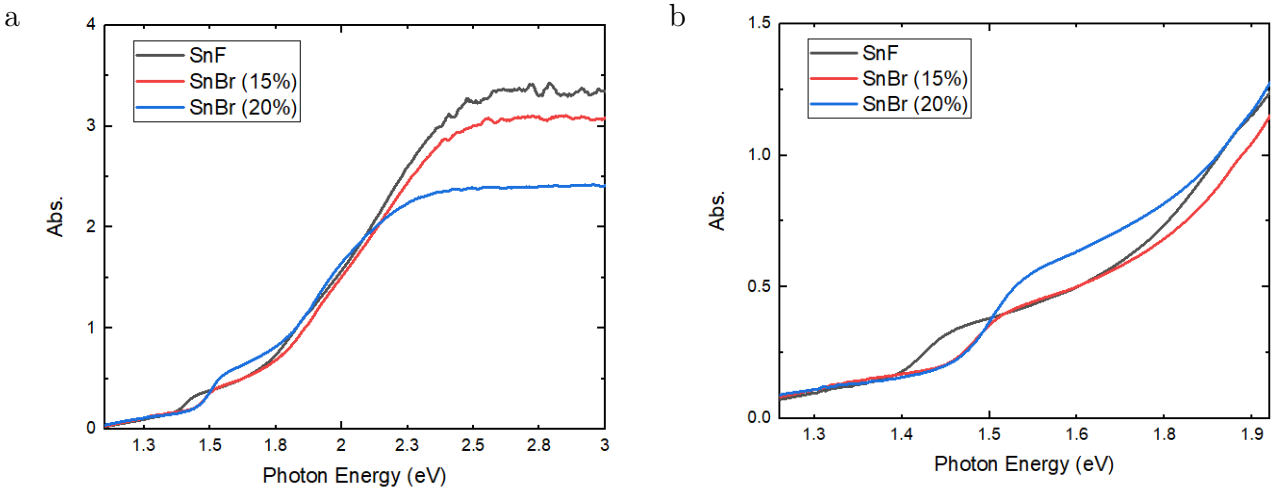

Figure 4.6: Absorbance spectra for the second batch of 3D perovskites.

The absorption of the 3D perovskites are shown in figures 4.5 and 4.6 and the 2D/3D perovskites are shown in figure 4.7. There are unfortunately a number of artefacts within the spectra that appear to be sharp onsets namely around 1.4 eV and 1.6 eV in figure 4.5(b) and around 1.7 eV in figure 4.7(b). These artefacts are a result of measurement errors in the equipment.

The higher concentrations appear to have an effect on the absorption onset that appears around 1.5 eV in figures 4.5(b) and 4.6(b). This onset in the spectra is a result of suppression of the Burnstein-Moss effect [33]. The Burnstein-Moss effect changes the apparent bandgap of a material and occurs when states close to the band edges are populated (electrons in the conduction band and holes in the valence band). It is an undesirable effect at it can inhibit certain energies of photons from being absorbed. SnF_2 is useful additive to suppress this but it is unclear from the absorption spectra if $SnBr_2$ is also. In all the SnBr samples, the onset is blue shifted, the shift being more drastic with higher concentrations. As before with the shift in the PL spectra, the blue shift could either be as a result of the Burstein-Moss effect or an effect of the wider bandgap of bromide itself. More research is needed to establish this differentiation.

a

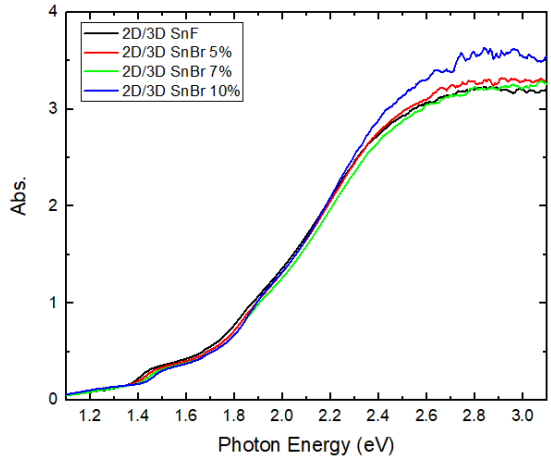

b

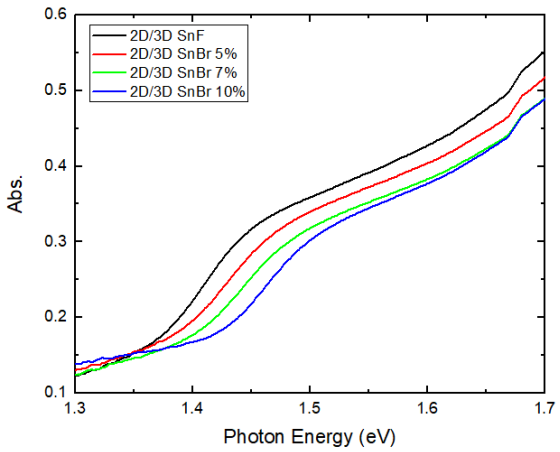

Figure 4.7: Absorbance spectra for the batch of 2D/3D perovskites.

As seen in figure 4.7 the blue shift is also present in the 2D/3D perovskites. Again it is unclear as to whether this shift is as a result of the Burstein-Moss effect or due to a contribution from the bromide halide.

4.4 XRD Measurements

To gather more information of the crystal structure of the perovskite and how it varies with these additives XRD measurements were taken. Figure 4.8 shows that XRD patterns matches that of a study on $FASnI_3$ from Shao *et al* which found "angles of 14.0°, 24.4°, 28.22°, 31.65°, 40.37° assigned to the crystallographic planes (100), (120)/(102), (200), (122), (222), respectively" [11]. All samples examined (SnF_2 and $SnBr_2$ 10% in both the 3D and 2D/3D regime) present peaks at angles 14.1°, 24.5°, 28.3°, 32°, 40.5° so it is likely that they similarly correspond to previosuly reported planes found in $FASnI_3$. 2D/3D SnBr 10% has additional peaks at 12° and 16°. Shao *et al* also found a peak around 12° when magnifying the range of 0-13° for 2D/3D perovskites. It's possible that they also found a peak at 16° but it was too small to appear in an non-magnified graph. As a result it is likely that these two additional peaks are a result of the additional planes created by the 2D/3D aspect of the crystal. However, these peaks are not found in 2D/3D SnF but that difference can be attributed to the higher noise level in that measurement that could be concealing their presence.

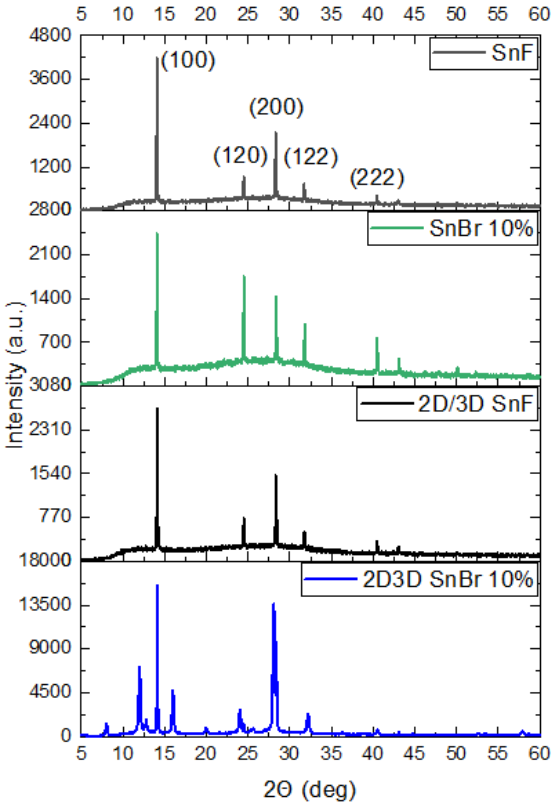

Figure 4.8: The XRD patterns of the 3D and 2D/3D perovskites with SnF and SnBr 10%. Labelled planes are taken from [11]. Data for this plot is courtesy of Eelco Tekelenburg.

Since the samples of $FASnI_3$ with additives SnF_2 and $SnBr_2$ appear to have the same crystal structure to a previously studied neat $FASnI_3$ it can be concluded that these additives do not have a strong influence on the crystal structure of the perovskite. This supports the intuitive understanding that small amounts of an alternative molecule does not heavily change the basic structure of the whole material.

By taking a closer look at the crystallographic planes, the kind of crystal structure the perovskite has can be determined. As previously stated, $FASn_3$ can have a cubic structure at room temperature. Using Bragg's Law 3.1 and A.3 a lattice constant of $a = 6.27$Å was found for plane (100) at 14.1°. This corresponds to previously reported lattice constants for cubic and pseudo-cubic phases of $FASn_3$. This confirms that the perovskite maintains it's cubic structure when containing SnF_2 or $SnBr_2$.

5 Conclusions

Tin halide perovskites have potential for high efficiencies but have a few issues hindering their performance: stability, self doping, reproducibility (as a result of their instability), and concerns of toxicity. Additives like SnF_2 have previously shown to help improve performance of the peroskite $FASnI_3$. Here using $SnBr_2$ as an additive, the surface morphology and optical properties were studied using SEM, photoluminescence, absorption, and XRD techniques to see if improvements in material quality could be obtained.. $SnBr_2$ was found to have some similar properties to SnF_2 as an additive when it comes to surface morphology, absorption, and crystal structure. The additive appears to form precipitates in the crystal structure of $FASnI_3$ when in excess, as SnF_2 also does. It also allows the perovskite to maintain its cubic structure apparent at room temperature. Interestingly, the surface morphology is slightly improved in samples with $SnBr_2$, at most in SnBr 5%, with larger grain sizes and fewer pinholes. Unfortunately, a shorter excited carrier lifetime (and as a result quicker hot carrier cooling) was shown in samples with $SnBr_2$ and so it can be concluded that $SnBr_2$ does not significantly improve material quality and performance in $FASnI_3$.

$SnBr_2$ should still be considered for use in other Sn-perovskites since it has shown promise in the inorganic $CsSnI_3$. It is yet unclear whether $SnBr_2$ is more beneficial in inorganic Sn-perovskites than organic ones so further research should not yet rule out using this additive in organic Sn-perovskites.

Acknowledgements

I would like to thank my daily supervisor Eelco for his guidance, advice, and kindness, I learned quite a lot from him. Thank you to Maria Loi and the POE group for their kindness and help, specifically Matteo and Eelco (again) for their SEM and XRD measurements. I also thank my mother and siblings for their support especially my sister Mairéad who, besides imploring me to talk much more about silicon semiconductors, had great advice. Finally I want to thank my late father David Scanlan, to whom this thesis is dedicated to, for being my one of my biggest supporters and for making this happen by funding my education.

References

[1] R. Wang *et al.*, "Prospects for metal halide perovskite-based tandem solar cells," *Nature Photonics*, vol. 15, 2021. [Online]. Available: https://www.nature.com/articles/s41566-021-00809-8

[2] "Best research-cell efficiency chart," *National Renewable Energy Laboratory, Golden, CO.*, 2022. [Online]. Available: https://www.nrel.gov/pv/cell-efficiency.html

[3] W. Shockley and H. J. Queisser, "Detailed balance limit of efficiency of p-n junction solar cells," *Journal of Applied Physics*, vol. 32, no. 510, 1961. [Online]. Available: https://doi.org/10.1063/1.1736034

[4] H. Min *et al.*, "Perovskite solar cells with atomically coherent interlayers on SnO 2 electrodes," *Nature*, vol. 598, no. 7881, pp. 444–450, 2021. [Online]. Available: https://pubmed.ncbi.nlm.nih.gov/34671136/

[5] K. Nishimura *et al.*, "Lead-free tin-halide perovskite solar cells with 13% efficiency," *Nano Energy*, vol. 74, no. 104858, 2020. [Online]. Available: https://doi.org/10.1016/j.nanoen.2020.104858

[6] A. Babayigit *et al.*, "Assessing the toxicity of Pb- and Sn-based perovskite solar cells in model organism danio rerio," *Scientific Reports*, vol. 6, no. 18721, 2016. [Online]. Available: https://doi.org/10.1038/srep18721

[7] F. Cima, "Tin: Environmental pollution and health effects," *Encyclopedia of Environmental Health 2nd ed.*, pp. 351–359, 2011. [Online]. Available: https://doi.org/10.1016/B978-0-12-409548-9.11198-4

[8] X. Jiang *et al.*, "Tin halide perovskite solar cells: An emerging thin-film photovoltaic technology," *Accounts of Materials Research*, vol. 2, no. 4, p. 210–219, 2021. [Online]. Available: https://doi.org/10.1021/accountsmr.0c00111

[9] X. Meng *et al.*, "Highly reproducible and efficient $FASnI_3$ perovskite solar cells fabricated with volatilizable reducing solvent," *Journal of Physical Chemistry Letters*, vol. 11, no. 8, p. 2965–2971, 2020. [Online]. Available: https://doi.org/10.1021/acs.jpclett.0c00923

[10] S. J. Lee *et al.*, "Fabrication of efficient formamidinium tin iodide perovskite solar cells through SnF_2-pyrazine complex," *Journal of The American Chemical Society*, vol. 138, no. 12, 2016. [Online]. Available: https://doi.org/10.1021/jacs.6b00142

[11] S. Shao *et al.*, "Highly reproducible Sn-based hybrid perovskite solar cells with 9% efficiency," *Advanced Energy Materials*, vol. 8, no. 4, p. 1702019, 2018. [Online]. Available: https://doi.org/10.1002/aenm.201702019

[12] S. Kahmann *et al.*, "Cooling, scattering, and recombination—the role of the material quality for the physics of tin halide perovskites," *Advanced Functional Materials*, vol. 29, no. 35, 2019. [Online]. Available: https://doi.org/10.1002/adfm.201902963

[13] J. H. Heo *et al.*, "Roles of SnX2 (X = F, Cl, Br) additives in tin-based halide perovskites toward highly efficient and stable lead-free perovskite solar cells," *Journal of Physical Chemistry Letters*, vol. 9, no. 20, p. 6024–6031, 2018. [Online]. Available: https://doi.org/10.1021/acs.jpclett.8b02555

[14] J. Y. Kim *et al.*, "High-efficiency perovskite cells," *Chemical Reviews*, vol. 120, pp. 7867–7918, 2020. [Online]. Available: https://doi.org/10.1021/acs.chemrev.0c00107

[15] S. Permogorov, "Hot excitons in semiconductors," *Physica Status Solidi (b)*, vol. 68, no. 9, 1975. [Online]. Available: https://doi.org/10.1002/pssb.2220680102

[16] I. Pelant and J. Valenta, *Luminescence Spectroscopy of Semiconductors*. Oxford University Press, 2012. [Online]. Available: https://doi.org/10.1093/acprof:oso/9780199588336.001.0001

[17] Q. Sun *et al.*, "Elucidating the unique hot carrier cooling in two-dimensional inorganic halide perovskites: The role of out-of-plane carrier–phonon coupling," *Nano Letters*, vol. 22, no. 7, p. 2995–3002, 2022. [Online]. Available: https://doi.org/10.1021/acs.nanolett.2c00203

[18] G. Kaur and H. N. Ghosh, "Hot carrier relaxation in $CsPbBr_3$-based perovskites: A polaron perspective," *Journal of Physical Chemistry Letters*, vol. 11, no. 20, pp. 8765–8776, 2020. [Online]. Available: https://doi.org/10.1021/acs.jpclett.0c02339

[19] G. Conibeer, D. König, M. Green, and J. Guillemoles, "Slowing of carrier cooling in hot carrier solar cells," *Thin Solid Films*, vol. 516, no. 20, 2008. [Online]. Available: https://doi.org/10.1016/j.tsf.2007.12.102

[20] S. Kahmann and M. A. Loi, "Hot carrier solar cells and the potential of perovskites for breaking the schocley-queisser limit," *Journal of Materials Chemitry C*, vol. 7, no. 9, 2019. [Online]. Available: https://pubs.rsc.org/en/content/articlelanding/2019/tc/c8tc04641g

[21] A. Chilvery *et al.*, "A perspective on the recent progress in solution-processed methods for highly efficient perovskite solar cells," *Science and Technology of Advanced Materials*, vol. 17, pp. 650–658, 10 2016. [Online]. Available: http://dx.doi.org/10.1080/14686996.2016.1226120

[22] M. Pitaro, E. K. Tekelenburg, S. Shao, and M. A. Loi, "Tin halide perovskites: From fundamental properties to solar cells," *Advanced Materials*, vol. 34, no. 1, 2022. [Online]. Available: https://doi.org/10.1002/adma.202105844

[23] T. Shi *et al.*, "Effects of organic cation on the defect physics of tin halide perovskites," *Journal of Materials Chemistry A*, vol. 5, no. 29, 2017. [Online]. Available: https://pubs.rsc.org/en/content/articlelanding/2017/TA/C7TA02662E

[24] S. Kahmann *et al.*, "Negative thermal quenching in $FASnI_3$ perovskite single crystals and thin films," *ACS Energy Letters*, vol. 5, no. 8, p. 2512–2519, 2020. [Online]. Available: https://doi.org/10.1021/acsenergylett.0c01166

[25] M. S. Ozório, M. Srikanth, R. Besse, and J. L. F. D. Silva, "The role of the A-cations in the polymorphic stability and optoelectronic properties of lead-free $ASnI_3$ perovskites," *Physical Chemistry Chemical Physics*, vol. 23, no. 3, pp. 2286–2297, 2021. [Online]. Available: https://doi.org/10.1039/D0CP06090A

[26] E.-B. Kim *et al.*, "A review on two-dimensional (2D) and 2D-3D multidimensional perovskite solar cells: Perovskites structures, stability, and photovoltaic performances," *Journal of Photochemistry and Photobiology C: Photochemistry Reviews*, vol. 48, p. 100405, 2021. [Online]. Available: https://doi.org/10.1016/j.jphotochemrev.2021.100405

[27] K. J. Savill, A. M. Ulatowski, and L. M. Herz, "Optoelectronic properties of tin–lead halide perovskites," *ACS Energy Letters*, vol. 6, pp. 2413–2426, 2021. [Online]. Available: http://dx.doi.org/10.1021/acsenergylett.1c00776

[28] S. Gupta *et al.*, "How SnF_2 impacts the material properties of lead-free tin perovskites," *Journal of Physical Chemistry*, vol. 122, no. 25, 2018. [Online]. Available: https://doi.org/10.1021/acs.jpcc.8b01045

[29] H. Sun *et al.*, "Strategies and methods for fabricating high quality metal halide perovskite thin films for solar cells," *Journal of Energy Chemistry*, vol. 60, pp. 300–333, 2021. [Online]. Available: https://www.sciencedirect.com/science/article/pii/S2095495621000140

[30] M. Nukunudompanich *et al.*, "Dominant effect of the grain size of the $MAPbI_3$ perovskite controlled by the surface roughness of TiO_2 on the performance of perovskite solar cells," *CrystEngComm*, vol. 11, no. 22, pp. 2718–2727, 2020. [Online]. Available: https://doi.org/10.1039/D0CE00169D

[31] S. Pachori *et al.*, "Fundamental physical properties of nontoxic tin-based formamidinium FASnX3 (X = I, Br, Cl) hybrid halide perovskites: Future opportunities in photovoltaic applications," *Energy Technology*, vol. 10, no. 2, p. 2100709. [Online]. Available: https://doi.org/10.1002/ente.202100709

[32] H.-H. Fang *et al.*, "Long-lived hot-carrier light emission and large blue shift in formamidinium tin triiodide perovskites," *Nature Communications*, vol. 9, no. 243, 2018. [Online]. Available: https://doi.org/10.1038/s41467-017-02684-w

[33] M. Grundmann, *The physics of semiconductors : an introduction including nanophysics and applications*. Springer, 2021. [Online]. Available: https://dx.doi.org/10.1007/978-3-030-51569-0

A Appendix

A.1 Finding lifetime from PL Time Resolve Spectra

The Time Resolve plots were fitted with an exponential graph starting from the peak and ending at the tail of the graph using the Nonlinear Curve Fit tool of OriginPro 2019b. The exponential formula denoted ExpDec2

$$y = y_0 + A_1 e^{-x/t_1} + A_2 e^{-x/t_2} \tag{A.1}$$

where y_0 is the offset, A_1, A_2 the amplitudes, and t_1, t_2 the decay constants. The total decay constant was found using

$$\tau = \frac{\sum_i (A_i t_i)^2}{\sum_i A_i t_i} \tag{A.2}$$

A.2 Determining Crystal Structure

For cubic structure the distance between adjacent planes d is

$$\frac{1}{d^2} = \frac{h^2 + k^2 + l^2}{a^2}. \tag{A.3}$$